



# Application of portable FTIR spectrometers for detecting greenhouse gas emissions of the major city Berlin

F. Hase<sup>1</sup>, M. Frey<sup>1</sup>, T. Blumenstock<sup>1</sup>, J. Groß<sup>1</sup>, M. Kiel<sup>1</sup>, R. Kohlhepp<sup>2</sup>, G. Mengistu Tsidu<sup>1,4</sup>, K. Schäfer<sup>3</sup>, M. K. Sha<sup>1</sup>, and J. Orphal<sup>1</sup>

<sup>1</sup>Karlsruhe Institute of Technology (KIT), Institute of Meteorology and Climate Research (IMK-ASF), Karlsruhe, Germany

<sup>2</sup>German Weather Service, Offenbach, Germany

<sup>3</sup>Karlsruhe Institute of Technology (KIT), Institute of Meteorology and Climate Research (IMK-IFU), Garmisch-Partenkirchen, Germany

<sup>4</sup>Department of Physics, Addis Ababa University, P.O. Box 1176, Addis Ababa, Ethiopia

Correspondence to: F. Hase (frank.hase@kit.edu)

Received: 19 February 2015 – Published in Atmos. Meas. Tech. Discuss.: 13 March 2015

Revised: 8 July 2015 – Accepted: 12 July 2015 – Published: 31 July 2015

**Abstract.** Five portable Bruker EM27/SUN FTIR (Fourier transform infrared) spectrometers have been used for the accurate and precise observation of column-averaged abundances of CO<sub>2</sub> and CH<sub>4</sub> around the major city Berlin. In the work by Frey et al. (2015), a calibration procedure is developed and applied to the set of spectrometers used for the Berlin campaign. Here, we describe the observational setup of the campaign and aspects of the data analysis, and we present the recorded time series of XCH<sub>4</sub> and XCO<sub>2</sub>. We demonstrate that the CO<sub>2</sub> emissions of Berlin can be clearly identified in the observations. A simple dispersion model is applied which indicates a total strength of the Berlin source of about 0.8 t CO<sub>2</sub> s<sup>-1</sup>. In the Supplement of this work, we provide the measured data set and auxiliary data. We hope that the model community will exploit this unique data set for state-of-the-art inversion studies of CO<sub>2</sub> and CH<sub>4</sub> sources in the Berlin area.

that they detect local variations and so are heavily influenced by local contributions and by details of the vertical mixing. Use of in situ measurements at different altitude levels (tall tower, aircraft) improves the representativeness considerably, but is a rather expensive approach. Current space-based remote-sensing observations are useful for the quantification of sources and sinks on continental scales but still suffer from limited precision, limited density of observations, and biases related to details of atmospheric scattering properties. Ground-based observations using high-resolution laboratory spectrometers as performed by TCCON (Total Carbon Column Observing Network; Wunch et al., 2011) can provide column-averaged abundances with reference precision and accuracy, but the number of sites is limited and the stations are not mobile. Portable FTIR spectrometers therefore are a very promising complement to current techniques, because they can probe larger sample volumes than in situ and smaller scales than current space-based sensors or globally distributed ground-based remote-sensing networks. In this work, we demonstrate the approach of using solar absorption spectra recorded with small low-resolution FTIR spectrometers at several sites distributed around a source region for an estimation of the encircled source strength.

The demonstration is based on a campaign we performed from 23 June to 11 July 2014 around Berlin using five spectrometers. We decided to target Berlin for several reasons. Firstly, Berlin is a major city, so we expect to measure detectable enhancements. Secondly, the city is relatively iso-

## 1 Introduction

The application of portable FTIR (Fourier transform infrared) spectrometers for the observation of column-averaged CO<sub>2</sub> and CH<sub>4</sub> abundances holds great promises with respect to the quantification of sources and sinks of greenhouse gases on regional and smaller scales. Although in situ measurements at the ground can be performed with unrivaled precision and accuracy, these measurements suffer from the fact

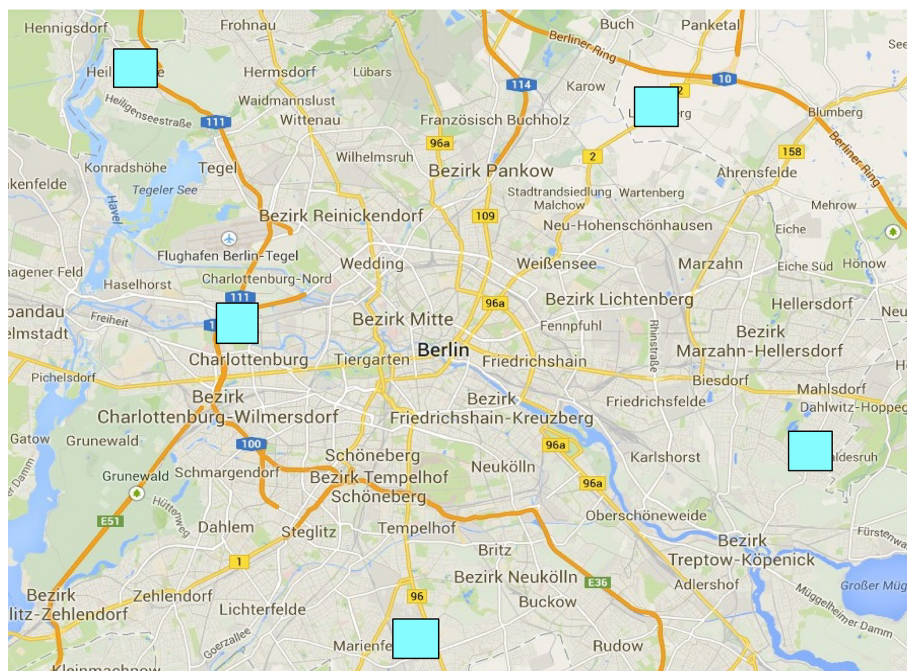


**Figure 1.** Map showing the measurement stations around Berlin.

**Table 1.** Geographical coordinates and altitudes of the measurement sites around Berlin. The coordinates were derived using GPS sensors. The reported altitudes result from combining time-averaged GPS measurements which were repeatedly performed at Mahlsdorf and average differences between the time series of ground pressures recorded at each site. Excellent agreement with topographic data provided on the website <http://www.wieweit.net> is found.

Site	Latitude ( $^{\circ}$ N)	Longitude ( $^{\circ}$ E)	Altitude (m)
Mahlsdorf	52.486	13.589	39.0
Charlottenburg	52.505	13.302	47.7
Heiligensee	52.622	13.228	34.5
Lindenberg	52.601	13.519	63.3
Lichtenrade	52.391	13.392	44.8

lated, so  $\text{CO}_2$  emissions really can be attributed to Berlin. Thirdly, the flat topography is favourable, which supports the interpretation of the recorded data. Measurements were performed at five different stations around Berlin, four of them roughly located along a circle with a radius of 12 km around the city centre of Berlin. One instrument was positioned inside the Berlin motorway ring in Charlottenburg, somewhat closer to the city centre than the other instruments. A map with all sites is shown in Fig. 1. The coordinates and altitudes of the different stations are displayed in Table 1. Due to somewhat unfavourable weather conditions, we were able to perform simultaneous measurements at all sites only on 10 days during the demonstration campaign. However, it should be noted that such spectrometers can be installed for

longer periods of operation in weather-resistant shelters and operated automatically – in order to form a permanent component of future monitoring systems.

Due to the long lifetimes of  $\text{CO}_2$  and  $\text{CH}_4$ , each individual source contribution is a weak signal superimposed on the average column-averaged background abundance. Therefore, ensuring a common calibration of all involved spectrometers and demonstrating their instrumental stability is of utmost importance for the proposed method. In Frey et al. (2015), a rigorous calibration procedure for the EM27/SUN spectrometer is developed and is exemplified using the set of portable spectrometers which we used for the Berlin campaign. This calibration procedure involved pre- and post-campaign measurements, thereby proving unambiguously the excellent instrumental stability of the devices.

## 2 Observational setup, weather, prevailing winds, and auxiliary measurements

Each site was equipped with an EM27/SUN spectrometer including a solar tracker, a GPS sensor used for accurate time-keeping, and a MHB-382SD data logger for recording pressure, temperature, and relative humidity. The measurement procedures (scan speed, resolution, numerical apodisation, etc.) applied during the campaign were chosen to be identical to those applied for the calibration measurements.

In Table 2, we collect the main characteristics of each measurement day. We list the number of observations available at each site and deduce a daily quality flag accord-

**Table 2.** Summary of all measurement days: number of observations at each site (Mahlsdorf, Charlottenburg, Heiligensee, Lindenberg, Lichtenrade), overall quality ranking of each day according to number of available observations and temporal coverage, ground wind speed and direction (classification from poor to excellent: o, +, ++, +++, +++++).

Date	No. of observations					Quality	Wind speed (m s <sup>-1</sup> )	Wind direction
26 Jun 2014 (Th)	76	70	89	28	116	+	2–4	NNE
27 Jun 2014 (Fr)	273	233	237	186	182	+++	5	SSW–SSE
28 Jun 2014 (Sa)	0	37	0	0	0	o	7	SSW
1 Jul 2014 (Tu)	203	189	158	122	224	++	8	W
2 Jul 2014 (We)	106	128	92	76	129	+	9	W
3 Jul 2014 (Th)	316	358	320	354	357	+++	7	W
4 Jul 2014 (Fr)	545	509	545	652	511	++++	7	SW–S
5 Jul 2014 (Sa)	0	93	0	0	0	o	5	SSW–SSE
6 Jul 2014 (Su)	329	265	346	252	385	++	5	W–SW
7 Jul 2014 (Mo)	10	74	28	98	130	+	8	SE–NW
8 Jul 2014 (Tu)	0	21	0	0	0	o	6	NE–E
9 Jul 2014 (We)	35	29	40	0	10	o	6–10	E–SSW
10 Jul 2014 (Th)	248	306	411	188	245	++	6–12–6	NE–E
11 Jul 2014 (Fr)	257	248	212	243	253	+	8	NE

ing to the overall data availability. Furthermore, the wind speeds and prevailing wind directions in the boundary layer are provided. The best measurement days with measurements throughout most of the day (solar elevation angle  $> 20^\circ$ ) were 27 June, 3 July and 4 July. During these days, prevailing winds were from the west (and south). Wind speeds were moderate in the range of 5 to 8 knots. Note that, although not very well covered, the set of observations includes a Sunday (6 July), which is an interesting aspect as a different temporal pattern and overall strength of emissions are expected on a Sunday than during a working day.

Very important auxiliary information required for the proper estimation of a source strength is the development of the boundary layer height during each day of observations. IMK-IFU performed continuous ceilometer measurements of the boundary layer height during the whole campaign period. The measurements were performed in Berlin-Neukölln (52.4895° N, 13.4309° E), 2.5 km to the southeast of the city centre. The ceilometer CL51 from Vaisala GmbH, Hamburg, Germany, is an eye-safe commercial mini-lidar system. Ceilometers detect initially the cloud height, but special software provides routine retrievals of up to five lifted layers from vertical profiles (vertical gradient) of laser backscatter density data (Münkel, 2007). In the absence of low clouds and precipitation and during scattered clouds, this measurement method estimates boundary layer height fairly well. The CL51 detects convective layer depths exceeding 2000 m and nocturnal stable layers down to 50 m. The measurement results agree well with those which are determined from profiles of relative humidity and virtual potential temperature measured by radiosonde (location of strong height gradient of aerosol backscatter density and relative humidity as well as temperature inversion; see Emeis et al., 2012). But radiosondes which are launched routinely twice per day only

do not provide sufficient information. Figure 2 shows the ceilometer results for 27 June: the developing boundary layer can be clearly seen, reaching an altitude of about 2200 m in the late afternoon. In the case of airborne particles it has been shown previously that boundary layer information as detected continuously by ceilometers enables the determination of near-surface concentrations from column density data (Schäfer et al., 2008).

### 3 The XH<sub>2</sub>O, XCO<sub>2</sub>, and XCH<sub>4</sub> time series

The analysis of the trace gases from the measured spectra has been performed as described by Gisi et al. (2012) and Frey et al. (2015). Because the distances between the sites are about 25 km or less, a common pressure–temperature profile has been used for the analysis at all sites. The pressure records of the MHB-382SD devices have been used to set the ground pressure values of the model atmosphere, and an intraday variability of the ground pressure and the temperature profile has been taken into account in the analysis of the spectra. For the construction of the temperature profiles, we utilize the NCEP model noon profiles provided by the Goddard autotailer system and radiosonde data provided by the meteorological observatory Lindenberg. We take the NCEP data as the starting values and overlap a linear ascent during the day, which is the temperature difference between the 00:00 and 18:00 LT sonde data, for the lowermost height levels (below 4 km altitude). For the height levels above 4 km we take the original NCEP noon data, as the change during the day is negligible.

Solar absorption spectral observations in the near infrared offer the potential of measuring column-averaged dry-air mole fractions with excellent precision and accuracy. This is owed to the facts that (1) scattering of photons into the line

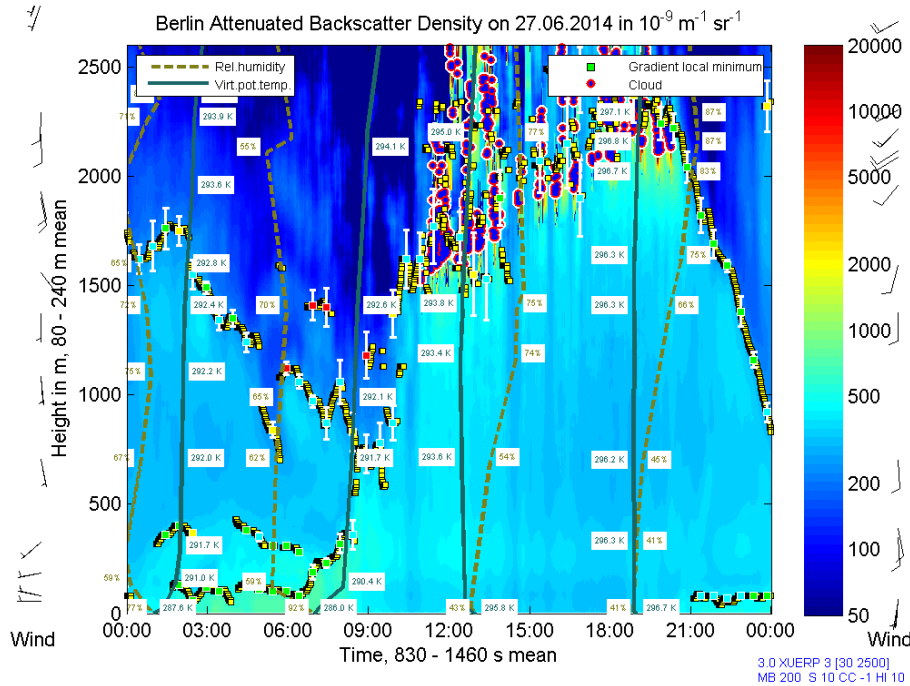


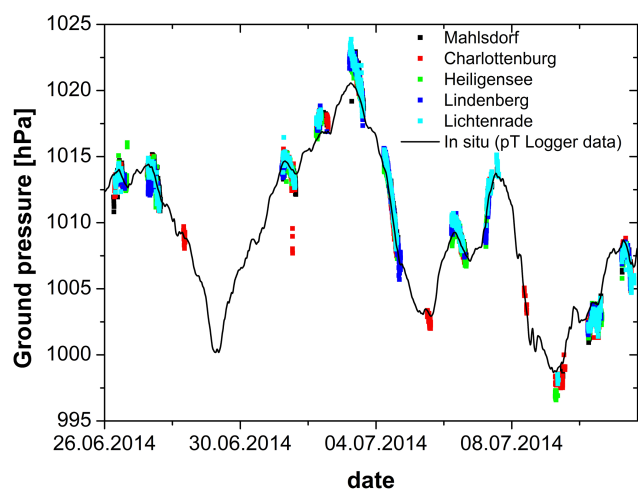
**Figure 2.** The development of the boundary layer thickness on 27 June according to ceilometer measurements performed by IMK-IFU in Berlin-Neukölln.

of sight is a negligible process and that (2) absorption bands of molecular oxygen are covered, so the column amount of oxygen can be derived from the same spectrum. Because the dry-air mole fraction of molecular oxygen is nearly invariable, the column-averaged dry-air mole fraction of the target gases can be derived from the ratio of the observed target gas columns and the oxygen column. This approach significantly reduces the impact of various error sources on the final results, because these typically affect both the target gas columns and the oxygen reference column (Wunch et al., 2011). Moreover, the amount of dry air deduced from the spectral information can be compared with the ground pressure measured with a barometer. Note that the barometer records the total ground pressure, including the pressure exerted by the water vapour column. However, this small contribution to the pressure can be taken into account in the comparison because the water vapour column can also be derived from the observed spectrum. Figure 3 shows the time series of the total ground pressure (derived from the average of the continuous barometer measurements performed with the MHB-382SD devices at all five sites) in comparison to the total ground pressures calculated from the spectral measurements (taking into account the water vapour contribution). The pressure values from the spectral measurements follow closely the variable ground pressure, and the agreement between different stations is excellent. A least-squares fit to the barometer data suggests a common calibration factor of 0.9713 for the spectroscopic measurements, which has

been applied in the figure. This result is in excellent agreement with the calibration factor found by Frey et al. (2015; 0.9700) and Klappenbach et al. (2015; 0.9717).

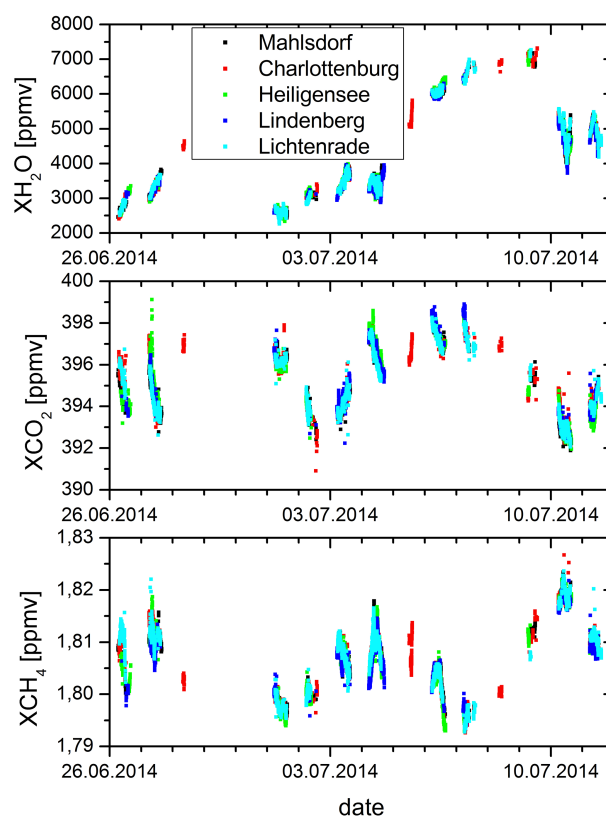
Figure 4 (top panel) shows the observed time series of  $\text{H}_2\text{O}$  dry-air mole fractions. As expected,  $\text{H}_2\text{O}$  varies considerably – by about a factor of 3 – over the campaign period. On the other hand, the agreement between the stations is surprisingly good. This demonstrates the uniform character of the selected area, especially the absence of localized dominating sources of atmospheric humidity, which would induce larger differences between the stations. Finally, as the main contribution to the  $\text{H}_2\text{O}$  total column originates from the boundary layer, this finding supports the assumption that the boundary layer across the whole probed area is well ventilated.

Figure 4 (middle and bottom panel) shows the  $\text{XCO}_2$  and  $\text{XCH}_4$  values (respectively) as observed by all spectrometers. The dominating synoptic variations which are common to all sites occur on timescales of several days. These variations of the order of 1 % peak to peak are due to the changing tropopause altitude and advection of air masses with different trace gas concentrations. In addition, the time series reveal intraday variability of the order of 0.5 % or less, which is variable from day to day, but also very similar in each individual data record. We assume that these variations result from a superposition of real variability and artefacts of the retrieval. During most of the observation days, a decrease of  $\text{XCO}_2$  is found, which is what would be expected as a result of photosynthetic activity during a sunny day (high



**Figure 3.** Time series of ground pressure according to the barometer measurements performed at each site (black line) and derived from the infrared spectra (dots). All pressure values were reduced to a common reference altitude of 30 m. For the spectroscopic results, the dry-ground pressure has been derived from the  $1.27\ \mu\text{m}$  oxygen band, and the contribution of water vapour to the total ground pressure has been taken into account. In order to achieve the best agreement with the barometer results, a calibration factor of 0.9713 has been applied to the spectroscopic results.

insulation being an obvious selection bias of solar absorption observations). On the other hand, variations symmetric around noon are particularly striking during a couple of days, mainly in the case of  $\text{CH}_4$ . It is plausible to assume an air-mass-dependent retrieval bias as a cause of these variations. We detailed in Frey et al. (2015) how we attempted to remove this artefact by applying an a posteriori air-mass-dependent correction. However, the observed bias is comprised of two contributions: one contribution resulting from forward-model errors (e.g. wrong line broadening parameters) – this tends to be a systematic feature and can be removed by the global correction we applied – and a second contribution due to the smoothing error of the retrieval. The column sensitivity of the scaling retrieval is a function of air mass, and so is the smoothing error. As described in Frey et al. (2015), we used constant a priori profile shapes in the retrievals, while the actual atmospheric profiles are variable. This gives rise to air-mass-dependent artefacts which are variable from day to day. Finally, on top of this variable background, subtle differences between individual observations can be detected: these are typically of the order of 1–2 %, and it is tempting to assume that these are caused by local emission contributions. For illustration, Fig. 5 shows the  $\text{XCH}_4$  and  $\text{XCO}_2$  values observed during 27 June. Southerly winds prevailed during that day, and indeed the  $\text{XCO}_2$  values observed in Heiligensee in the northwest of Berlin are elevated. It is important to note that, although the emission signals tend to be smaller than the observed intraday variability,



**Figure 4.** Evolution of  $\text{XH}_2\text{O}$  (top panel),  $\text{XCO}_2$  (middle panel), and  $\text{XCH}_4$  (bottom panel) as measured at all sites during the campaign.

enhancements as small as 0.5 % are noticeable. This is possible because the detection of an enhancement can be based on the differences between the column-averaged mole fractions observed at different sites, if these are superimposed on a smoothly varying background traced by the observations of several upstream stations. This situation is realized if all sites observe similar advected larger-scale variations. Note that at a given time during the day all sites perform measurements under nearly the same solar elevation angle and quite similar atmospheric conditions (atmospheric vertical profile shapes of trace gases). This reduces significantly retrieval biases between the stations, especially if the interpretation of the collected data is mainly based on differences between simultaneous observations of upstream and downstream stations. In detail, the observed  $\text{XCH}_4$  enhancements differ from the  $\text{XCO}_2$  enhancements, which is expected due to different sources. Moreover, the background of the  $\text{XCH}_4$  seems less well defined and more variable. This meets the expectation: due to the likely presence of rural  $\text{CH}_4$  sources around the conurbation area encircled with the stations and due to the stronger contrast between tropospheric and stratospheric mixing ratios of  $\text{CH}_4$ , higher variability is expected in the  $\text{XCH}_4$  background field than in case of  $\text{XCO}_2$ . We feel that a sensible investigation of our  $\text{XCH}_4$  observations would re-

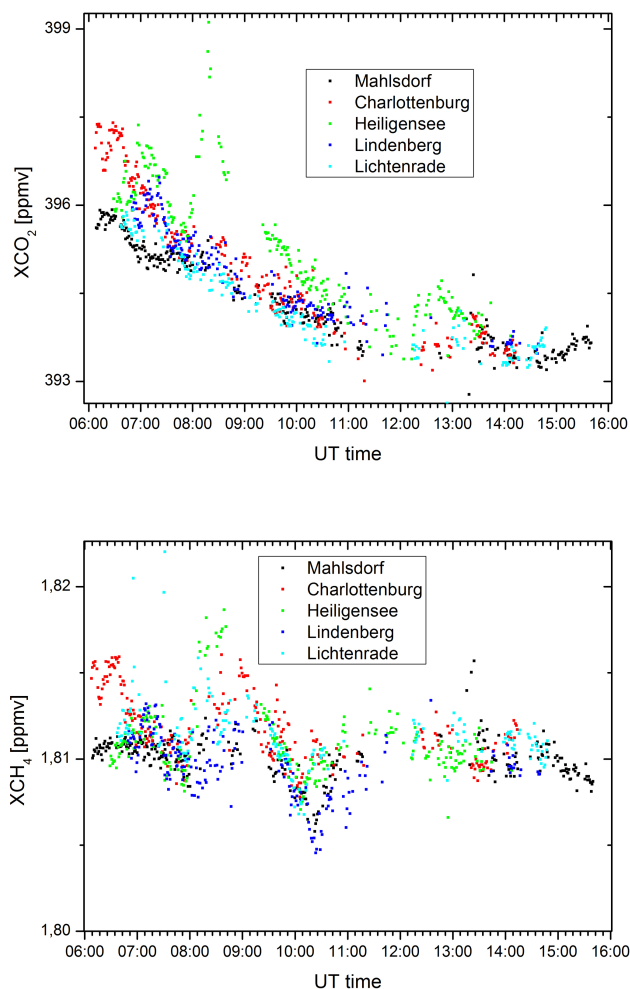


**Figure 5.** Observed variability of  $XCH_4$  and  $XCO_2$  during 27 June 2014.

quire a state-of-the-art high-resolution inversion model, and we hope that the data sets made available in the Supplement to this work will be exploited in depth by the inverse model community. Using a simple dispersion model, we will in the following focus on a more specific interpretation of the observed  $XCO_2$  enhancements. In the next section, we describe the main characteristics of the dispersion model. In Sect. 5 we compare observations and model predictions.

#### 4 Setup of a simple dispersion model

For a prediction of the differences in  $XCO_2$  between sites we have created a simple dispersion model. Within this modelling scheme, the Berlin source is mapped into a schematic area source spanned by five neighbouring rectangles, which contribute to the total source strength. The central rectangle reflects the city centre; the four remaining rectangles reflect Charlottenburg and Spandau areas (western box), Reinickendorf and Pankow areas (north-

**Table 3.** The five emission regions used in the dispersion model. The last row provides the percentage contribution to the total emission strength of the Berlin source as assumed in the model.

Box ID	Area	NW corner	SE corner	% contribution
1	Charlottenburg and Spandau	52.5677 13.0753	52.5159 13.2550	25
2	Tempelhof-Schöneberg	52.4657 13.2304	52.3800 13.4275	15
3	Marzahn-Hellersdorf and Treptow-Köpenick	52.5531 13.4502	52.3927 13.6316	10
4	Reinickendorf and Pankow	52.6302 13.3046	52.5472 13.4721	10
5	City centre	52.5472 13.2550	52.4657 13.4502	40

ern box), Marzahn-Hellersdorf and Treptow-Köpenick areas (eastern/south-eastern box), and the Tempelhof-Schöneberg area (southern box). The geographical coordinates of each box and the percentage contribution to the total emission are listed in Table 3. The spatial extent and contribution of each box have been adjusted according to information on population and traffic density provided by the Statistical Office of Berlin-Brandenburg (<http://www.stadtentwicklung.berlin.de>).

The dispersion model uses analysed hourly horizontal wind fields from COSMO-DE, the convective-scale regional component of the numerical weather prediction system of the German Weather Service (DWD; Baldauf et al., 2011). Due to the fact that we assume a distributed source region, we do not apply the COSMO wind field at full resolution, which is of the order of  $2.8 \times 2.8$  km, but use only five COSMO hourly wind profiles distributed over the observation area (in the centre and the NW, NE, SW, and SE corners of a square centred on Berlin with an edge length of about 20 km) and interpolate the winds between these reference wind profiles linearly through time and – assuming a Shepard inverse distance weighting with a power of 2 (Shepard, 1968) – on a horizontal plane.

The model is based on a strict Lagrangian perspective. It does not use a model grid but instead transports emitted particles according to the interpolated winds at their current locations. The generation rate of the particles is proportional to the source strength; they are created at the ground level within one of the five emission regions described before. For each creation act, the region is selected by a random generator in accordance with the assumed contribution of the region; the starting position within the selected area is again chosen randomly. Within a selected region, the probability of emission is equal for each area element; we do not attempt to resolve sources on a scale smaller than the source region.

Concerning the vertical transport, a fast mixing on timescales of  $\sim 10$  min across the whole boundary layer is assumed. This is realized in the model by introducing a fast

erratic diffusion of each particle along the vertical axis. The altitude limit of the model boundary layer is for each day chosen in accordance with ceilometer measurements. Fast fluctuations of the boundary layer thickness detected by the ceilometer are neglected; instead the individual overall development of the boundary layer height during each day is approximated using piecewise linear fits.

Finally, the detection of particles is emulated by checking whether the particle is inside a cylinder which wraps the line of sight of one of the observation sites. It should be noted that due to the daily apparent motion of the sun in the sky, the position of this cylinder is quite variable. If we assume a boundary layer thickness of 1500 m and start and end of observations at a solar elevation angle of  $20^\circ$ , then the top surface of the cylinder is shifted by 8 km westwards during the day, which is not negligible in comparison to the extent of the assumed source regions. Therefore, the line of sight used for the detection condition is updated in the model according to the astronomical conditions.

The simulation period starts at midnight. In each time step (1 s), a particle is emitted and all existing particles are transported. During daytime, as long as the solar elevation exceeds  $20^\circ$ , the number of detected particles at each observation site is determined in intervals of 450 s. Typically, depending on wind speed, 20 000–40 000 particles are traced at a given time (each emitted particle is followed for up to a distance of 40 km from the Berlin centre). The simulation run for each day is repeated 500 times and the results are averaged to achieve a negligible statistical noise in the number of detection counts. Note that the model does not take into account emissions from the previous day. Typically, these aged emissions have left the region of interest before, but occasionally – if the wind speed is very low – it might happen that they reside for longer than 6 h in the observed area, or may return from outside the modelled area if the wind direction is changing. No attempt is made in the dispersion calculation to include the variable advected XCO<sub>2</sub> background; it only predicts the enhancements at each observation site due to the daily emissions of the local Berlin source.

## 5 Comparison of predicted and observed time series

In the following, we compare the XCO<sub>2</sub> measurements with results from the dispersion model for the three most favourable observation days. For all days, the Berlin CO<sub>2</sub> source strength was fixed to a plausible value of  $800 \text{ kg CO}_2 \text{ s}^{-1}$ . The source strength was kept constant during the day, although one would certainly expect considerable intraday variability for different kinds of contributions, e.g. traffic peaking at around 08:00 and 17:00 (local time). Figures 6–8 show the observational and model results for 27 June, 3 July, and 4 July. For the first 2 days, the model enhancements are shown superimposed on a smooth polynomial background, which is reasonably well defined by the observations of the

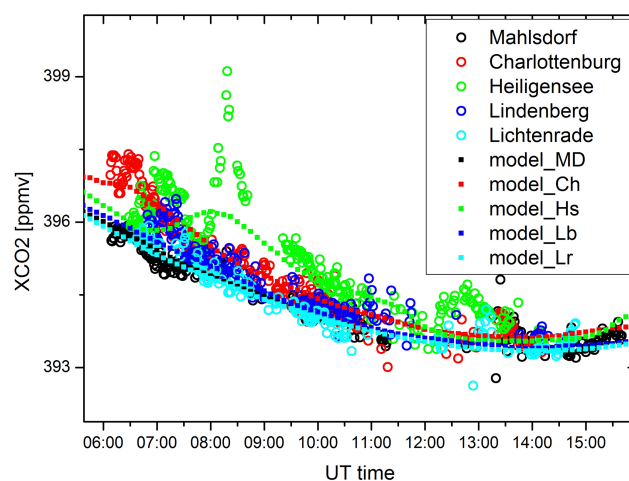


**Figure 6.** Observed and modelled XCO<sub>2</sub> for 27 June. The model enhancements are shown superimposed on a smooth polynomial background which has been derived from the observations of the upstream stations.

upstream stations. During the 3rd day, 4 July, it is more difficult to estimate a smooth background level as all stations, including the upstream stations, observe considerable variability. Therefore, for this day the predicted enhancements are shown superimposed on a constant 390 ppm background level.

The model prediction for 27 June is of acceptable quality. The enhancements before noon observed first in Charlottenburg and afterwards in Heiligensee are well captured. The peak at 0.35 day fraction observed in Heiligensee is much sharper than the model prediction and indicates a significant contribution of a localized source smaller than the assumed emission regions. Southerly winds prevailed during the day, so this source is probably located in model region 1. Indeed, the heat- and power-generating coal-fired plant Reuter West operated by Vattenfall AB with a peak thermal power of 774 MW (<http://kraftwerke.vattenfall.de/powerplant/reuter-west>) is located in this region and is the likely source of the observed emissions. Afterwards, the model predicts elevated values for Heiligensee until around noon, which is in good agreement with the observations, but it fails to predict the final enhancement observed in Heiligensee after noontime.

For 3 July, the enhancements are smaller than those observed during 27 June. Still, the undulations predicted by the model are detectable in the Lindenberg time series reasonably well, although the first two peaks are underestimated and appear delayed in the model simulation by about half an hour. The final increase towards the third peak observed in the afternoon is nicely reproduced. The model predicts slightly higher values for Mahlsdorf than for Heiligensee and Lichtenrade, which is not supported by the observations, which instead indicate repeated peaks in the Heiligensee and

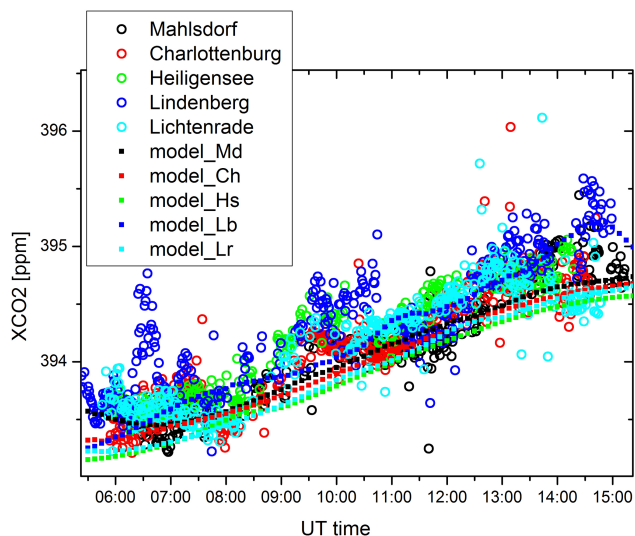


**Figure 7.** Observed and modelled  $XCO_2$  for 3 July. The model enhancements are shown superimposed on a smooth polynomial background which has been derived from the observations of the upstream stations.

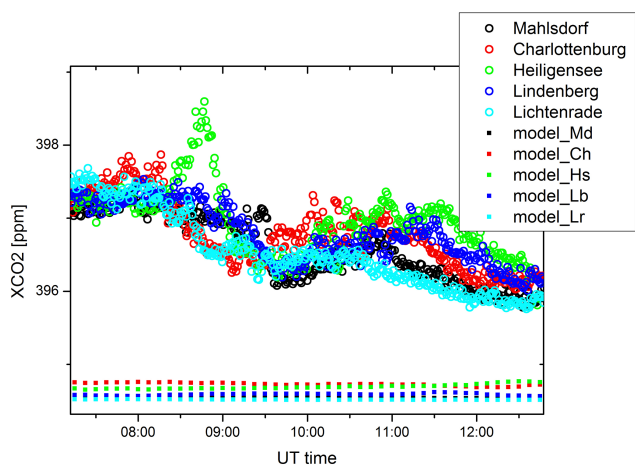


**Figure 8.** Observed and modelled  $XCO_2$  for 4 July. Due to the high variability of the upstream values observed during this day, no attempt has been made to construct a common background value.

Lichtenrade time series. Westerly winds were prevailing during that day, so for the station Lichtenrade emissions from Potsdam (not included in the model) are likely to contribute.

For 4 July, the observed  $XCO_2$  values are quite variable. An M-shaped disturbance extending over 5 h and observed at all stations before noon is the most prominent feature. Southerly winds prevailed near the ground and southwesterly winds in the free troposphere. While a similar shape is observed at all stations, there is a clear time lag of about 45 min between the occurrence of this disturbance between the upstream stations (Lichtenrade and Charlottenburg) and the downstream stations (Heiligensee and Lindenberg). This

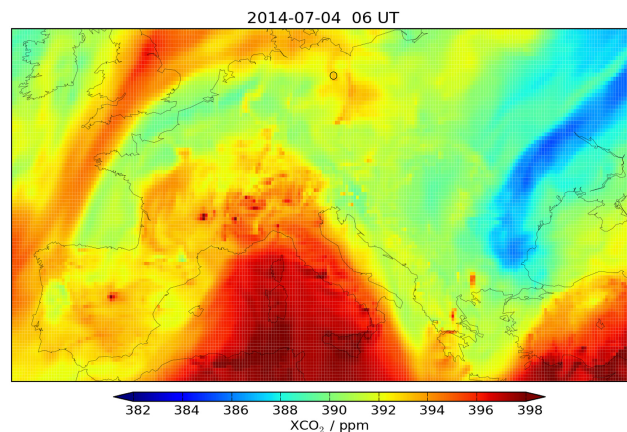


**Figure 9.**  $XCO_2$  distribution according to the MACC model across central Europe for the morning of 4 July. North is up; orientation marks are superimposed along the continental coastlines (dark lines). The open circle denotes the location of Berlin.

time lag agrees well with the delay expected for the advection of a disturbance in the background  $XCO_2$  signal at a wind speed of about  $7 \text{ m s}^{-1}$  across a distance of about 20 km between the sites. The variations between the stations are too strong to allow a judgement concerning the model prediction of a 0.5 ppm enhancement at Heiligensee and Charlottenburg.

Figure 9 shows the MACC (Monitoring Atmospheric Composition & Climate project) prediction for  $XCO_2$ . A closer examination of the previous development of the  $XCO_2$  field according to MACC indicates that the complex structures in the  $XCO_2$  field around Berlin during that day are possibly the result of an entrainment of emissions from western Germany and further sources nearer to Berlin. The example of 4 July demonstrates the limitations of a simple dispersion model which takes into account only the local sources. A comprehensive exploitation of the information contained in the kind of measurements presented here would require state-of-the-art inverse modelling allowing for a resolved local source distribution nested into a much wider model area. Such a model configuration would include a reasonable description of variations due to advected  $XCO_2$  contributions from outside the model area and associated larger-scale variations of column-averaged abundances.

## 6 Data set provided in the Supplement

In the Supplement to this work, we provide the complete set of quality-filtered  $XCH_4$  and  $XCO_2$  observations collected during the campaign at all stations. The quality filter is based on the quality of the interferograms (average value and fluctuation of the DC value). For each site, we provide the apparent solar elevation angle of the measurement, the retrieved total column amount of  $H_2O$ , and the  $XCH_4$  and  $XCO_2$  cali-

brated with respect to TCCON and corrected for the systematic spurious air mass dependence (column-averaged dry-air mole fractions in ppm). In separate tables, we provide the a priori profile shapes of CH<sub>4</sub> and CO<sub>2</sub> used for the scaling retrieval on the 49 model levels of the retrieval code (dry-air mole fractions in ppm) and the averaging kernel matrices with dimensions of 49 × 49 for different solar zenith angles. These auxiliary data enable the user to estimate the smoothing error of the column-averaged abundances, especially the impact of the actual profile shape on XCH<sub>4</sub> and XCO<sub>2</sub>. If the user wants to include the smoothing characteristics of the remote-sensing observations in the comparison between observations and assimilation model, we suggest including the kernel convolution directly in the model predictor. In addition to the FTIR data, the Supplement contains the results derived from the ceilometer observations in both tabulated and graphical form.

## 7 Summary and outlook

We presented measurements of column-averaged abundances of CH<sub>4</sub> and CO<sub>2</sub> recorded with five portable FTIR spectrometers during a measurement campaign of 3 weeks' duration around Berlin in summer 2014. The results demonstrate that an array of well-calibrated, ground-based FTIR spectrometers allow the reliable detection of XCH<sub>4</sub> and XCO<sub>2</sub> enhancements due to local emissions in the range of 1%. Application of a simple dispersion model indicates that the observations are compatible with an assumed source strength of the order of 800 kg CO<sub>2</sub> s<sup>-1</sup> for the major city Berlin. We believe that arrays formed with such spectrometers would be a very useful complement to existing in situ and remote-sensing measurements for the quantification of sources and sinks of CH<sub>4</sub> and CO<sub>2</sub> on regional scales. We expect that a comprehensive inversion of local source contributions to the observed column-averaged abundances will require state-of-the-art nested model approaches which include a proper description of the variable advected background contributions. Such model studies could also be of great value for the design of monitoring networks (density and locations of stations) based on portable FTIR spectrometers.

**The Supplement related to this article is available online at doi:10.5194/amt-8-3059-2015-supplement.**

*Acknowledgements.* We acknowledge support by the ACROSS research infrastructure of the Helmholtz Association.

We thank the National Center for Environmental Prediction (NCEP) for providing atmospheric temperature profiles via the Goddard automailer system.

We acknowledge the availability of XCO<sub>2</sub> maps from MACC-III. MACC-III is a Coordination & Support Action (2014–2015) funded by the European Union under the Horizon 2020 Programme, coordinated by the European Centre for Medium-Range Weather Forecasts and operated by a 36-member consortium. Further project details can be found at <http://www.gmes-atmosphere.eu>. Andre Butz, KIT, kindly prepared the plot based on MACC-III data.

We are very thankful for the successful cooperation during the measurement campaign “Berlin Air quality and Ecosystem Research: Local and long-range Impact of anthropogenic and Natural hydrocarbons” (BAERLIN2014), and especially the coordinators Boris Bonn and Erika von Schneidemesser, Institute for Advanced Sustainability Studies e.V., Potsdam, Germany.

We thank the German Weather Service (DWD) for providing the COSMO-DE analysis data which were used for the wind profiles in the dispersion model.

We acknowledge support by Deutsche Forschungsgemeinschaft and Open Access Publishing Fund of the Karlsruhe Institute of Technology.

The article processing charges for this open-access publication were covered by a Research Centre of the Helmholtz Association.

Edited by: J. Notholt

## References

- Baldauf, M., Seifert, A., Förstner, J., Majewski, D., Raschendorfer, M., and Reinhardt, T.: Operational convective-scale numerical weather prediction with the COSMO model: description and sensitivities, *Mon. Weather Rev.*, 139, 3887–3905, doi:10.1175/MWR-D-10-05013.1, 2011.
- Emeis, S., Schäfer, K., Münkler, C., Friedl, R., and Suppan, P.: Evaluation of the interpretation of ceilometer data with RASS and radiosonde data, *Bound-Lay. Meteorol.*, 143, 25–35, 2012.
- Frey, M., Hase, F., Blumenstock, T., Groß, J., Kiel, M., Mengistu Tsidu, G., Schäfer, K., Sha, K. M., and Orphal, J.: Calibration and instrumental line shape characterization of a set of portable FTIR spectrometers for detecting greenhouse gas emissions, *Atmos. Meas. Tech.*, 8, 3047–3057, doi:10.5194/amt-8-3047-2015, 2015.
- Gisi, M., Hase, F., Dohe, S., Blumenstock, T., Simon, A., and Keens, A.: XCO<sub>2</sub>-measurements with a tabletop FTS using solar absorption spectroscopy, *Atmos. Meas. Tech.*, 5, 2969–2980, doi:10.5194/amt-5-2969-2012, 2012.
- Klappenbach, F., M. Bertle, J. Kostinek, F. Hase, T. Blumenstock, A. Agusti-Panareda, M. Razinger and A. Butz: Accurate mobile remote sensing of XCO<sub>2</sub> and XCH<sub>4</sub> latitudinal transects from aboard a research vessel, *Atmos. Meas. Tech.*, in press, 2015.
- Münkler, C.: Mixing height determination with lidar ceilometers – results from Helsinki Testbed, *Meteorol. Z.*, 16, 451–459, 2007.

Schäfer, K., Harbusch, A., Emeis, S., Koepke, P., and Wiegner, M.: Correlation of aerosol mass near the ground with aerosol optical depth during two seasons in Munich, *Atmos. Environ.*, 42, 4036–4046, 2008.

Shepard, D.: Proceedings of the 1968 ACM National Conference, 517–524, 23rd ACM National Conference, Las Vegas, NV, USA, 27–29 August 1968, doi:10.1145/800186.810616, 1968.

Wunch, D., Toon, G. C., Blavier, J.-F. L., Washenfelder, R. A., Notholt, J., Connor, B. J., Griffith, D. W. T., Sherlock, V., and Wennberg, P. O.: The Total Carbon Column Observing Network, *Philos. T. R. Soc. A*, 369, 2087–2112, doi:10.1098/rsta.2010.0240, 2011.